Shuaida Li, Yue Jun, Zhang Yang*

INVESTIGATION OF SURFACE TEXTURING FOR ENHANCING THE ANTI-VIBRATION SUPPORT STRUCTURE OF HEAT EXCHANGER TUBES

ISTRAŽIVANJE POVRŠINSKE TEKSTURE U CILJU POBOLJŠANJA ANTI-VIBRACIONE NOSEĆE KONSTRUKCIJE CEVI IZMENJIVAČA TOPLOTE

Originalni naučni rad / Original scientific paper
Rad primljen / Paper received: 23.02.2026
https://doi.org/10.69644/ivk-2026-siA-0075

Adresa autora / Author's address:
College of Mechanical Engineering, Zhejiang University of Technology, Hangzhou, China *email: zhoumingjue@zjut.edu.cn

Keywords
- surface texturing
- flow-induced vibration
- heat exchanger tube
- impact wear

Abstract

Flow-induced vibration (FIV) often causes wear between heat exchanger (HE) tubes of steam generators (SGs) and their support structures, such as anti-vibration bars (AVBs), which in turn compromises the structural integrity and operational safety of the nuclear power system. To mitigate this issue, this study proposes the use of laser surface texturing (LST) to enhance the wear resistance of AVBs. Micro-textures with different geometries and area densities are fabricated on AVB surfaces using femtosecond laser processing. Series of impact-wear tests are conducted in both water and air environments to simulate friction process under actual operating conditions. The results indicate that the water environment not only effectively suppresses stress but also extends the wear location along the axial direction of the HE tube, preventing the wear depth from rapidly penetrating the tube wall thickness. The primary wear mechanisms in the water environment are identified as fatigue wear and oxidative wear, differing from the fatigue-abrasive composite wear mechanism observed in air. A conversion method for wear volume between the two environments is also established. This study confirms that surface texturing is an effective method for extending the lifespan of HE tubes and enhancing their structural integrity.

Ključne reči
- površinsko teksturisanje
- vibracije izazvane strujanjem (fluidima)
- cev razmenjivača toplote
- habanje usled udara

Izvod

Vibracije izazvane strujanjem često uzrokuju habanje između cevi razmenjivača toplote parogeneratora i njihovih potpornih konstrukcija, kao što su antivibracione poluge AVB, što posledično ugrožava integritet konstrukcije i pogonsku bezbednost nuklearnog energetskog sistema. U cilju ublažavanja ovog problema, u radu se predlaže primena laserskog teksturisanja površine kako bi se povećala otpornost na habanje antivibracionih poluga. Mikroteksture različitih geometrija i površinskih gustina izrađene su na površinama AVB-a pomoću femtosekundne laserske obrade. Sprovedena je serija ispitivanja udarnog habanja u vodenoj i vazdušnoj sredini kako bi se simulirao proces trenja u realnim radnim uslovima. Rezultati pokazuju da vodena sredina ne samo da efikasno potiskuje napon, već i proširuje zonu habanja duž aksijalnog pravca cevi razmenjivača toplote, sprečavajući da dubina habanja brzo probije debljinu zida cevi. Utvrđeno je da su primarni mehanizmi habanja u vodenoj sredini zamorno habanje i oksidaciono habanje, što se razlikuje od kombinovanog mehanizma zamorno-abrazivnog habanja uočenog u vazduhu. Uspostavljena je i metoda konverzije zapremine habanja između ove dve sredine. Potvrđuje se da je površinsko teksturisanje efikasno za produženje radnog veka cevi razmenjivača i za unapređenje integriteta.

INTRODUCTION

The global transition toward sustainable energy has positioned nuclear power as an indispensable alternative to fossil fuels, offering a reliable and scalable clean energy source. Within the complex architecture of a Pressurised Water Reactor (PWR), the steam generator (SG) serves as the critical interface between the primary nuclear heat source and the secondary power-generating turbines.

Consequently, the operational safety of the entire nuclear system is fundamentally dependent on the structural integrity of thousands of internal U-shaped heat exchanger tubes. Historical data and failure analyses indicate that tube degradation remains a leading cause of unscheduled plant outages /1-2/. Catastrophic incidents, such as the 1991 failure at the Mihama Nuclear Power Plant and the 2012 leakage at the San Onofre Nuclear Generating Station, underscore the severe consequences of tube perforation, /3/.

The primary mechanism driving this degradation is flow-induced vibration (FIV). As the high-velocity, high-temperature secondary coolant flows across the densely packed tube bundles, it generates complex hydrodynamic forces. These fluid-structure interactions are governed by several distinct phenomena, including vortex shedding, fluid-elastic instability, and random turbulent buffeting, /4-5/. Due to thermal expansion and manufacturing tolerances, minute physical clearances between the heat exchanger tubes and their structural supports - specifically the anti-vibration bars (AVBs) and tube support plates - are unavoidable. Consequently, fluid-induced oscillations force the tubes into repetitive, high-frequency contact with these supports. This dynamic interaction induces complex impact-sliding fretting wear, characterised by simultaneous normal impact forces and tangential sliding friction, /6-7/.

Over decades of operation, such repetitive dynamic loading causes highly localised stress concentrations, progressive material removal, wall thinning, and eventual tube perforation, /8/.

To mitigate these corrosion-related failures, modern heat exchanger tubes predominantly utilise Inconel 690, a nickel-based superalloy renowned for its exceptional resistance to primary water stress corrosion cracking and high-temperature oxidation. However, extensive metallurgical and tribological investigations reveal that its fretting wear behaviour remains highly sensitive to operational variables, such as normal contact loads, displacement amplitudes, excitation frequencies, and environmental temperatures, /9-10/. In elevated-temperature aqueous environments, the wear mechanisms of Inconel 690 transition intricately among adhesive wear, abrasive ploughing, fatigue-induced delamination, and oxidative tribo-corrosion. This complex evolution depends heavily on localised fluid dynamics and contact stress severity, /11-12/. Although high-temperature water provides a degree of boundary lubrication and facilitates debris removal, it also introduces a severe synergistic effect between continuous mechanical wear and electrochemical corrosion. This synergy rapidly degrades the protective chromium oxide passivation layer, exposing the nascent substrate to accelerated fatigue failure, /13/. Furthermore, recent predictive studies utilising machine learning models have confirmed that variations in impact frequency heavily dictate the ultimate damage response of the alloy surface, /14/.

While considerable scientific effort has focused on altering the bulk metallurgy of heat exchanger tubes or adjusting the macroscopic geometry and clearance tolerances of the support structures, relatively few studies have explored the implementation of targeted, micro-scale surface modifications on the anti-vibration bars themselves. Recently, surface texturing has garnered significant attention in the fields of advanced tribology and structural engineering as a highly effective, non-intrusive method for controlling friction, mitigating wear, and enhancing the structural lifespan of dynamically loaded components /15-16/. By artificially fabricating specific, highly controlled micro-geometries, such as dimples, grooves, or cross-hatches, on a contacting surface, researchers have demonstrated enhanced hydrodynamic lift, improved localised fluid cooling, and the creation of micro-reservoirs that effectively trap and sequester abrasive wear debris, /17-18/.

Among the various techniques available for surface modification, femtosecond laser surface texturing is particularly advantageous, representing the vanguard of modern micro-machining, /19/. Utilising ultra-short pulses (typically in the femtosecond range) and extraordinarily high instantaneous peak power, these lasers facilitate a process known as ‘cold ablation’ /20/. Unlike continuous-wave or long-pulse nanosecond lasers, the femtosecond pulse duration is shorter than the electron-phonon relaxation time of the metallic lattice. Consequently, the material is rapidly ionised and ejected as a plasma plume before thermal energy can diffuse into the surrounding bulk material. This unique physical mechanism allows for the creation of incredibly precise micro-dimples or complex hierarchical topographies without inducing detrimental thermal residual stresses, micro-cracking, or extensive heat-affected zones (HAZ) in the substrate, thereby preserving the fundamental structural integrity of the component, /21-22/.

Despite the proven efficacy of femtosecond LST in extending the operational lifespan of automotive engine cylinders, aerospace thrust bearings, and biomedical implants, its specific application to the highly aggressive, fluid-immersed impact-sliding fretting conditions of nuclear heat exchangers remains largely unexplored. The complex tribological interplay among the micro-textured stainless steel surface, the pressurised aqueous medium, and oscillating nickel-based superalloy tube requires rigorous empirical quantification to validate its feasibility as a life-extension strategy.

Therefore, this study systematically investigates the efficacy of femtosecond laser-induced micro-textures on 405 stainless steel anti-vibration bars in mitigating the impact-sliding fretting wear of Inconel 690 tubes. By methodically varying both the geometrical morphology (evaluating circular dimples, square pits, and equilateral triangular pits) and the surface area density of the textures (ranging from 5 % to 24.2 %), this research seeks to identify the optimal surface parameters required to maximise structural protection. Furthermore, by executing extensive comparative experimental trials in both ambient air and fully submerged water environments, this study provides critical insights into the environmental dependence of the component's degradation mechanisms. Ultimately, this research provides actionable, data-driven methodologies to enhance the reliability, safety, and longevity of critical nuclear power generation infrastructure.

MATERIALS AND EXPERIMENTAL METHODS

To achieve a comprehensive understanding of tribological and structural interactions between the heat exchanger tubes and micro-textured anti-vibration bars, a rigorously controlled experimental framework is established. This methodology encompasses the precise characterisation of the raw materials, the mathematical and physical parameters of the femtosecond laser ablation process, the structural dynamic modal analysis of the testing assembly, and the execution of high-frequency impact-sliding wear tests in diverse environmental conditions.

Specimens and metallurgical characterisation

Primary structural specimens utilised in this empirical investigation are specifically selected to mimic the exact material pairings currently deployed in contemporary PWR steam generators. The dynamic heat exchanger tube specimens are sectioned from nuclear-grade, thermally treated Inconel 690 alloy thin-walled tubes, procured from Baoyin Special Steel Tube Co., Ltd. The geometric specifications of the tube specimens are strictly controlled, featuring an outer diameter of 17.48 mm, a wall thickness of 1.01 mm, and a functional testing length of 400 mm. Inconel 690 is an austenitic nickel-chromium-iron superalloy, heavily favoured in nuclear applications due to its high chromium content, which imparts exceptional resistance to oxidising chemicals and high-temperature stress-corrosion cracking.

The opposing static friction pair, representing the anti-vibration bar (AVB) support structure, consists of 405 stainless steel blocks precisely machined to dimensions of 18 mm × 12.19 mm × 10 mm. This ferritic stainless steel is commonly utilised for structural supports due to its lower coefficient of thermal expansion and adequate corrosion resist-

ance. Prior to the commencement of the laser texturing and wear testing phases, the elemental compositions of both alloys are empirically verified to ensure compliance with nuclear standards. The compositional analysis is conducted utilising a BRUKER S1 TITAN 500 hand-held X-ray fluorescence (XRF) spectrometer for metallic elements, and a LECO CS844 infrared carbon sulphur analyser for non-metallic inclusions. The exact weight percentages of the constituent elements for both the Inconel 690 tubes and the 405 stainless steel AVBs are detailed in Table 1.

Table 1. Chemical composition of samples (wt.%).

Component	Ni	Cr	Fe	Si	Mn
Inconel 690 Alloy	58.46	30.16	10.36	0.28	0.44
405 Stainless Steel	0.09	13.50	84.90	0.41	0.57

Surface texture design and fabrication

Surface texturing is an advanced strategy to optimise tribological performance without altering the bulk material. Its core function is to capture wear debris and inhibit three-body abrasion by constructing specific surface geometries.

For example, Vandoni et al. /23/ used laser processing to create micro-dimples with a depth of less than 2 μm.

Research confirms that these micro-textures serve a dual role as 'oil reservoirs' and 'debris traps' during friction: they act as lubricant reservoirs for continuous replenishment and effectively capture wear particles during relative slip, thereby significantly mitigating abrasive wear.

The tribological effects of a texture are closely related to its geometric parameters, including morphology, size, arrangement, and area density, /24/. Generally, increasing the texture density can reduce the real contact area, which helps to lower the friction coefficient. Furthermore, the influence mechanisms of texture depth and size differ under dry friction and lubricated conditions. For this reason, three geometric shapes are designed to characterise the surface texture regions as shown in Fig. 1.

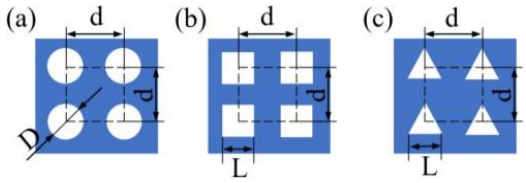

Figure 1. Schematic diagram for calculating micro-texture surface density: a) circular dimple micro-texture; b) square pit micro-texture; c) equilateral triangular pit micro-texture.

The area density of the circular dimple surface texture can be calculated by Eq.(1):

$$\rho = \frac{\pi D}{4d^2} \cdot 100\ \%, \tag{1}$$

where: ρ is area density (%); D is diameter of the circular dimple (μm); and d is spacing of dimples in the horizontal and vertical directions (μm).

The area density of the square pit surface texture can be calculated by Eq.(2):

$$\rho = \frac{L}{d^2} \cdot 100\ \%, \tag{2}$$

where: ρ is area density (%); L is side length of the square pit (μm); and d is the spacing (μm).

The area density of the triangular pit surface texture can be calculated by Eq.(3):

$$\rho = \frac{\sqrt{3L^2}}{4d^2} \cdot 100\ \% \tag{3}$$

where: ρ is area density (%); L is side length of triangular pit (μm); and d is the spacing (μm).

Femtosecond Laser Fabrication: the experimental substrate is 405 stainless steel AVB. To remove surface impurities and oxides, all samples are ultrasonically cleaned in 99 % anhydrous ethanol for 10 minutes before processing, and then removed and air-dried.

Femtosecond laser processing platform (GY-LC-03) is used to fabricate dimple-type micro-textures on the 405 stainless steel substrate. Laser processing is performed over an area of 18 mm × 12.19 mm. Detailed laser process parameters are shown in Table 2.

Table 2. Femtosecond laser parameters.

Laser power [W]	Pulse frequency [kHz]	Scan speed [mm/s]	Laser spot size [μm]	Max single pulse energy [J]	Scan Passes (times)
3	500	900	10	300	300

In this study, 3 dimple texture morphologies (circular, square, triangular, Fig. 2, are designed (Table 3). The area density (S_p) for all textures is controlled at 10 %, the dimple depth is designed to be 15.0 μm, and spacing is 280 μm. After processing, samples are ultrasonically cleaned again to remove debris and slag generated during ablation.

Table 3. Dimensions of microtextured anti-vibration bars.

Morphology	Size L/D [μm]	Pitch P [μm]	Depth h [μm]	Area s [μm^2]	Density %
Circular	100	280	15.0	7854	(1)
Square	88.62	280	15.0	7854	(2)
Triangular	134.68	280	15.0	7854	(3)

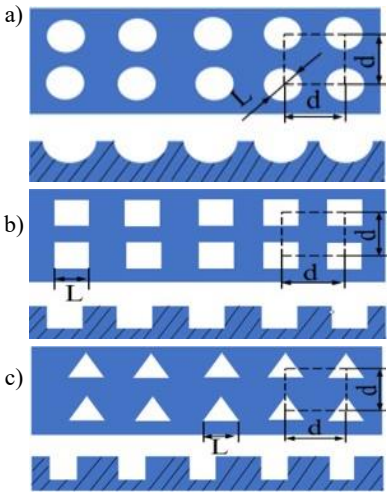

Figure 2. a) Circular dimple; b) square pit; c) triangular pit.

Post-ablation, the specimens are re-subjected to ultrasonic cleaning to remove any loosely adhered re-deposited nanoparticles or oxide debris generated by the plasma plume. The resulting surface topographies are extensively characterised using a Keyence VK-X3000 series laser confocal shape measurement microscope that verifies that the femtosecond

laser successfully produces sharp, well-defined vertical sidewalls with negligible thermal distortion or residual melt lips.

Structural dynamics and modal analysis of the testing assembly

To ensure that experimental wear testing accurately replicates the authentic flow-induced vibration conditions of a steam generator, the structural dynamics of the testing assembly require rigorous validation. Flow-induced vibration forces the tubes to oscillate at specific frequencies; if the testing apparatus are to inadvertently operate at the natural resonant frequency of the tube, the resulting catastrophic amplitude spikes would invalidate the wear data.

Therefore, a preliminary modal analysis is conducted to determine the natural frequencies and the dynamic stiffness of the tube-support structure. The analytical framework relies on the Euler-Bernoulli beam theory. For a tube with one end rigidly fixed and the other end free, the theoretical natural frequency (f_n) is calculated by:

$$f_n = \frac{\beta_n^2}{2\pi L^2}\sqrt{\frac{EI}{\rho A}}, \tag{4}$$

where: β_n is eigenvalue corresponding to boundary conditions (for a cantilever, $\beta_n = 1.875$); L is effective length; E is elastic modulus (2.11×10^5 MPa for Inconel 690), ρ is material density (8190 kg/m^3); A is cross-sectional area; and I is cross-sectional moment of inertia, calculated for a hollow cylinder as:

$$I = \frac{\pi(D^4 - d^4)}{64}. \tag{5}$$

By using the solid 188 beam element in ANSYS®, a finite element model of 690 alloy heat exchange tube is established. One end fixed support constraint is applied, one end is free, and one end is fixed support and one end simple support constraint on both ends of the heat exchange tube for modal analysis. At the same time, the subspace method is used to extract the first 5 natural frequencies of the heat exchange tube. Figures 3 and 4 show the simulation results of the first 2 natural frequencies of the heat exchange tube under two different constraint conditions.

To transition from theoretical models to empirical validation, a vibration response testing platform is constructed, utilising a Siemens LMS SCADAS Mobile SCM2E05 data acquisition system and a 504AF02 acceleration sensor. A dynamic impact hammer is used to apply a transient excitation force to the Inconel 690 tube under varying boundary conditions. Furthermore, ANSYS solid 188 beam elements are utilised to perform a finite element (FE) modal simulation. The comparative results of the theoretical calculations, the finite element simulations, and empirical impact hammer tests are presented in Table 4.

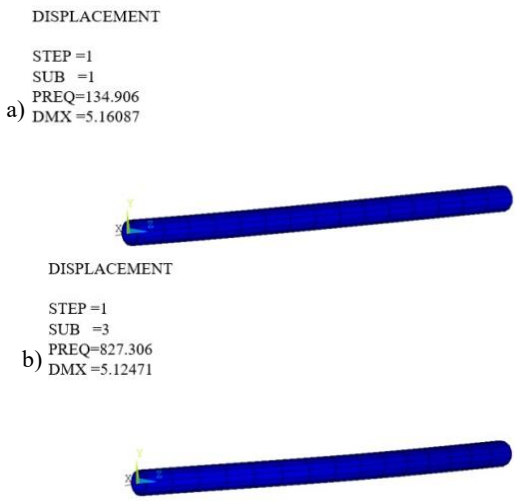

Figure 3. Simulation results of natural frequencies for a structure with one end fixed and the other end free: a) first-order natural frequency; b) second-order natural frequency.

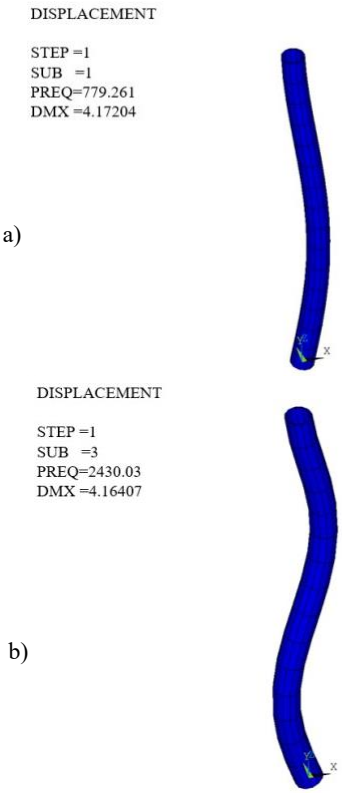

Figure 4. Simulation results of natural frequencies for a structure with one end fixed and the other end simply supported: a) first-order natural frequency; b) second-order natural frequency.

The empirical first-order natural frequency of the specific testing configuration (fixed at the top, supported by the dual AVBs at the bottom) is measured at 356.59 Hz. This value lies perfectly between the extremes of the completely free

Table 4. Comparison of theoretical, finite element, and empirical natural frequencies for Inconel 690 tube under varying boundary constraints.

Category	Fixed-free		Fixed-simply supported		Fixed-AVB supported	
	1st order (Hz)	2nd order (Hz)	1st order (Hz)	2nd order (Hz)	1st order (Hz)	2nd order (Hz)
Theoretical value	135.25	847.68	809.07	2621.97	/	/
FEM simulated value	134.91	827.31	779.26	2430.03	/	/
Experimental value	114.29	/	/	/	356.59	468.39

and the rigidly simply-supported boundary conditions, confirming that the designed AVB fixture provides a highly realistic, semi-rigid dynamic stiffness constraint. Based on this modal data, the operational excitation frequency for all subsequent impact-sliding wear tests is strictly set to a constant 70 Hz. This frequency is sufficiently distant from the fundamental resonant mode to prevent chaotic resonance, while adequately representing the high-frequency turbulent buffeting characteristic of PWR secondary flow.

Structural dynamics and modal analysis of testing assembly

The core impact-sliding fretting wear experiments are executed on a custom-engineered, multi-environment vibration testing platform. As illustrated in the apparatus schematic (Fig. 5), the vertical architecture of rig centres around a heavy-duty structural column. The Inconel 690 heat exchanger tube is mounted vertically parallel to this column, with its upper terminus rigidly fixed by a dedicated tube support bracket to eliminate parasitic frame compliance. An ES-1-150 electromagnetic vibration exciter, positioned adjacently, delivers highly precise, computer-controlled sinusoidal dynamic loads. This exciter is coupled to the tube via a 5 mm diameter 304 stainless steel excitation rod. At the lower testing interface, the apparatus features a specialised force sensor support and water tank assembly. Within this assembly, the paired AVB specimens are mounted. The excitation force is applied at an angle of 45° relative to the AVB mounting bracket, causing the tube to undergo a complex, bi-directional orbital motion that forces it to impact and slide against the AVBs located 50 mm from the lower free end of the tube. To simulate the submerged aqueous environment, a transparent glass containment cover is installed over the contact zone, securely resting on the bottom water tank support base, which allows for full fluid immersion of the friction pair while enabling visual monitoring.

To accurately simulate the physical clearances resulting from manufacturing tolerances and thermal expansion in an actual steam generator, the total diametral gap between the Inconel 690 tube and paired 405 stainless steel AVBs is meticulously calibrated to exactly 0.2 mm using high-precision wedge feeler gauges.

Experiments are systematically divided into two distinct environmental conditions to isolate the effects of the fluid medium. Initial baseline tests are conducted in ambient room-temperature air. Subsequently, a specially designed transparent acrylic containment vessel, sealed with high-grade structural silicone, is utilised to completely submerge the tube-AVB contact interface in high-purity distilled water. Distilled water is deliberately selected over chemically treated reactor coolant to isolate the purely mechanical and hydrodynamic effects of the fluid medium from complex chemical corrosion variables.

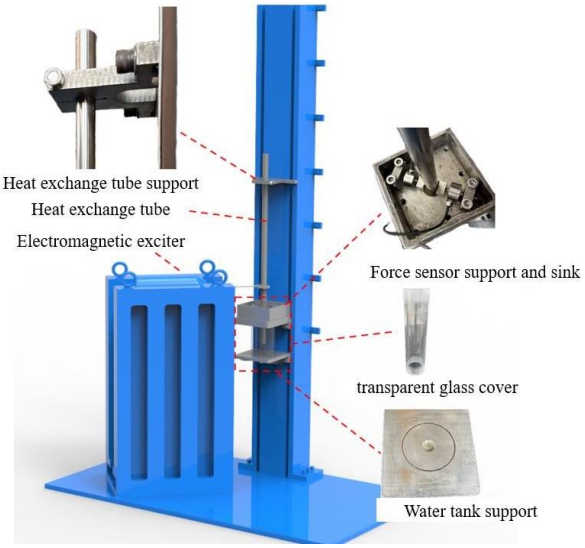

Figure 5. Physical picture of wear test device.

The dynamic loading protocol applied a constant 70 Hz sinusoidal excitation signal. As detailed in the system schematic, the experimental operation is governed by an integrated closed-loop control and data acquisition architecture. The desired excitation parameters are programmed via the master computer and transmitted to IM1608 controller. This control signal is subsequently boosted by a DA-1020-65 power amplifier - maintained by a dedicated cooling system to ensure thermal stability during extended operation - to actuate the vibration exciter coupled to the 400 mm heat exchanger tube (Fig. 6). To evaluate the effect of varying kinetic energy inputs, the excitation load (F) is incrementally tested at 40 N, 50 N, 60 N, and 70 N. Each individual test block is run continuously for a duration of 8 hours, resulting in approximately 2.016×10^6 impact-sliding cycles per specimen.

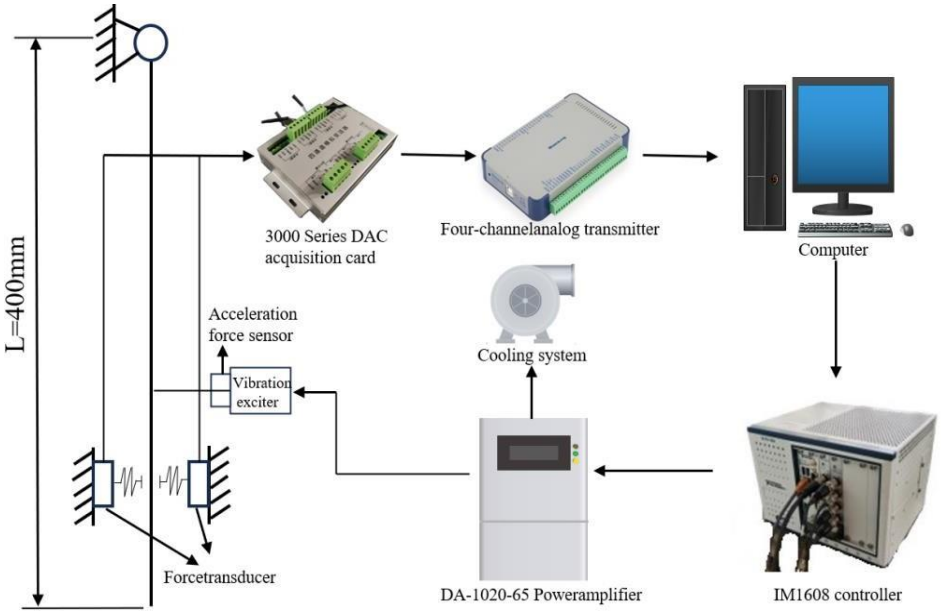

Figure 6. Flowchart of the wear test principle.

To capture the highly transient structural responses and collision events, force transducers are integrated directly behind the AVB mounts (functioning as the lower spring-supported fixed constraints), while an acceleration force sensor is mounted adjacent to the vibration exciter. The analogue signals from these precise sensors are routed sequentially through a 3000 Series DAC acquisition card and a four-channel analogue transmitter before being continuously logged and processed by the computer. Operating at a high sampling rate of 125,000 samples per second, this robust acquisition framework ensures the high-fidelity resolution of the micro-second impact peaks.

RESULTS AND DISCUSSION

Empirical data derived from the extensive experimental matrix reveal highly complex, multi-variable interactions between the dynamic excitation forces, the environmental medium, and the micro-topography of support structures. This section systematically dissects these interactions, progressing from baseline surface characterisation to advanced predictive wear modelling and micro-mechanical failure analysis.

Topographical and mechanical evolution of femtosecond laser-textured surface

The application of femtosecond laser surface texturing fundamentally alters both the micro-geometry and localised mechanical properties of the 405 stainless steel AVB substrate. To precisely quantify these topographical transformations, a Bruker NPFLEX 3D optical nano-surface interferometer is employed for high-resolution baseline and post-ablation metrology. As illustrated in the metrology setup, the system comprises the main interferometry unit coupled with a dedicated data analysis workstation (Fig. 7a). During the measurement process, the precisely machined 405 stainless steel AVB block is firmly secured on a highly stable, perforated sample stage.

This configuration allows the high-magnification objective lens, positioned directly above the sample, to perform non-contact optical profiling of the micro-scale surface topography (Fig. 7b). Utilising this advanced equipment, the baseline metrology establishes that the conventionally polished, smooth AVB possesses an initial average surface roughness R_a = 0.99 μm. As anticipated, the introduction of laser-ablated micro-dimples drastically increases the global surface roughness, with the magnitude of increase scaling proportionally to the applied texture area density.

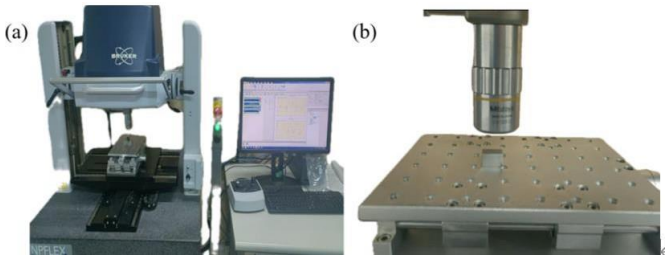

Figure 7. Nano-surface Interferometer: a) appearance of the equipment; b) observation platform.

To provide an intuitive visualisation of this topographical evolution, the two-dimensional pseudo-colour contour maps and their associated statistical roughness parameters are analysed in detail. Figure 8a illustrates the baseline smooth surface, exhibiting a uniform profile characterised by minor polishing marks and a minimal average roughness R_a = 873.62 nm. Figures 8(b-f) depict the array of circular micro-dimples engineered at varying surface area densities. In these optical profiles, the deep blue circular zones correspond to the laser-ablated cavities, which contrast sharply with the red and orange regions representing the pristine, load-bearing plateaus. Topographical maps clearly display configurations with 5 % (Fig. 8b), 10 % (Fig. 8d), 14.8 % (Fig. 8c), 19.6 % (Fig. 8e), and 24.2 % (Fig. 8f) texture densities. A direct correlation is visually and statistically evident: as structural density of the dimple array increases, there is a systematic escalation in all primary roughness metrics, including R_a, root-mean-square roughness R_q, and maximal peak-to-valley height R_t. This optical characterisation unequivocally confirms that the macroscopic surface asperity profile is a direct geometric consequence of the femtosecond laser's volumetric ablation density.

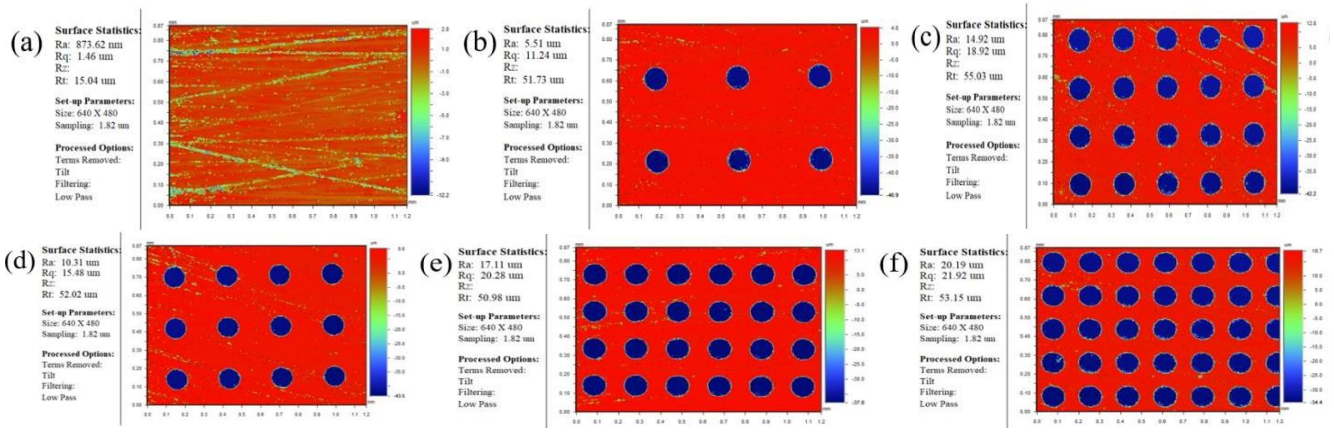

Figure 8. Roughness of the second batch of anti-vibration strips: a) smooth surface; b) circular pits with 5 % texturing rate; c) circular pits with 10 % texturing rate; d) circular pits with 14.8 % texturing rate; e) circular pits with 19.6 % texturing rate; f) circular pits with 24.2 % texturing rate.

As detailed in Table 5, the surface roughness exhibits a strong dependence on both the micro-texture morphology and the area density. For the circular dimple configuration, the average roughness R_a increases proportionally with the texture density. Starting from a smooth baseline of 0.99 μm, the R_a rises to 5.67 μm at a minimal 5 % density, and surges dramatically to 20.45 μm at the maximal tested density of 24.2 % - representing an extraordinary roughness amplification of over 1965 % relative to the smooth baseline. Furthermore, a comparative analysis of the different morphologies engineered at a constant 10 % density reveals that geometric shape significantly impacts surface topography. While the 10 % circular dimple yields R_a = 10.00 μm, the equivalent 10 % square pit results in a substantially higher R_a = 20.88 μm. This critical finding indicates that at an identical ablation area density, the sharp corners and straight edges of square pits induce much more severe localised topographical variations than continuous, smooth perimeters of circular dimples.

Table 5. Surface roughness of micro-textured surface morphologies.

Surface morphology	Rough. 1 (μm)	Rough. 2 (μm)	Rough. 3 (μm)	Average
Smooth surface	0.87	1.08	1.04	0.99
Circular-5% density	5.51	5.92	5.58	5.67
Circular-10% density	10.31	9.64	10.06	10.00
Square-10% density	20.41	21.58	20.65	20.88
Circular-14.8% density	14.92	15.09	15.06	15.02
Circular-19.6% density	17.11	17.06	16.61	16.92
Circular-24.2% density	20.08	21.09	20.19	20.45

Beyond topographical alterations, the femtosecond laser ablation induced significant micro-metallurgical transformations. Vickers microhardness testing conducted in the immediate peripheral vicinity of the ablated dimples reveals an average hardness increase of 9.47 %, elevating the bulk material hardness from 233.56 to 255.7 HV. This localised hardening is a direct consequence of the extreme thermal dynamics inherent to femtosecond ablation. Although the overall heat-affected zone (HAZ) is minimal compared to continuous-wave lasers, the extraordinarily rapid, localised thermal shock followed by instantaneous quenching precipitates severe microstructural grain refinement and dislocation entanglement at the ablation boundary. From a structural integrity perspective, this hardened peripheral matrix acts as a reinforced load-bearing plateau, theoretically enhancing the material's resistance to initial plastic yielding and localised asperity crushing under severe impact-sliding loads.

Environmental influence on dynamic contact forces and fluid-structure interaction

The transition from a dry, ambient air environment to a fully submerged aqueous environment introduces a profound paradigm shift in the structural dynamic response of the heat exchanger assembly. As visually captured in the continuous time-domain force monitoring over the 30,000 second (approximately 8-hour) test cycles, there is a consistent, counter-intuitive amplification of impact forces when the system is submerged in water.

To mitigate this fluid-induced force amplification, the influence of surface texturing on the dynamic contact forces is systematically evaluated. As illustrated in the cyclic impact force curves (Fig. 9a) and the average and maximal impact force (Fig. 8b), introducing circular micro-dimples at varying surface area densities (5 %, 14.8 %, 19.6 %, and 24.2 %) significantly alters the contact mechanics under the maximal 70 N excitation load in water. The data reveals that the micro-textured surfaces possess a pronounced capability to regulate impact intensity. The average impact force drops to a minimum of 32.24 N at 19.6 % texture density. However, the maximal transient impact force exhibits a counter-trend, peaking near 40.76 N at the 19.6 % density before dropping to its absolute minimum of approximately 37.81 N at the maximal tested density of 24.2 %. This divergence indicates that while intermediate texture densities are effective at reducing steady-state sliding resistance, the highest texture density (24.2 %) provides the optimal structural damping and fluid-cushioning effect required to successfully suppress the most severe, instantaneous impact peaks during high-frequency collisions.

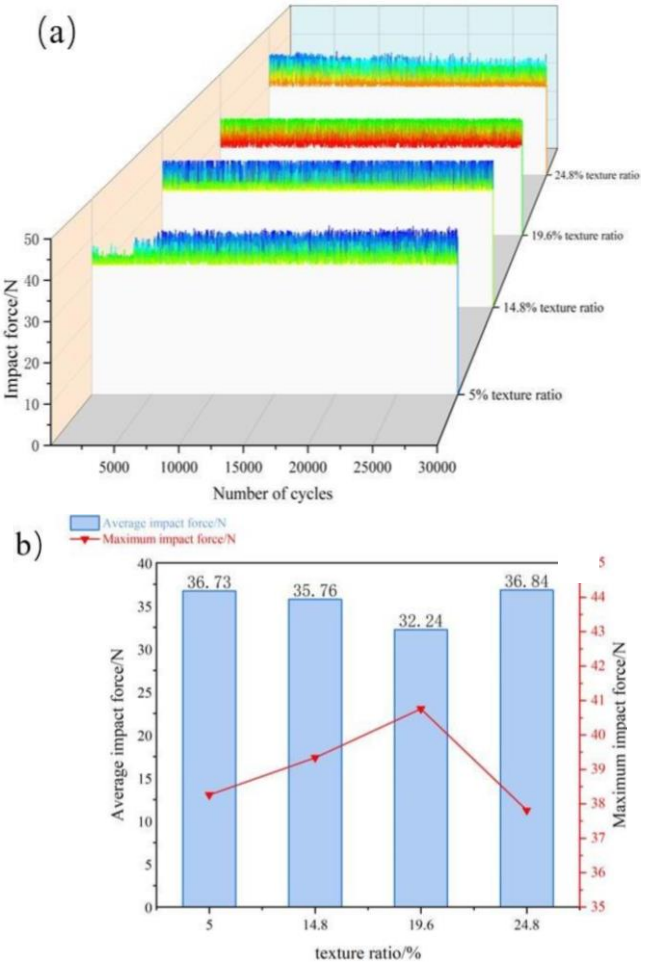

Figure 9. Impact force characteristics under different texture ratios: (a) cyclic impact force curves; (b) average and max. impact force

As documented in Table 6, across the entire spectrum of applied excitation loads (40 to 70 N), the peak dynamic contact forces recorded at the tube-AVB interface were significantly higher in the water environment. For instance, at a baseline excitation of 40 N, the maximal contact force

in air was 18.01 N, whereas in water, it escalated to 21.39 N (an 18.77 % increase). At the maximum excitation load of 70 N, the disparity widens further, with the air environment yielding a 37.27 N impact, while the water environment records a massive 46.48 N peak force, a 27.71 % amplification.

This force amplification is fundamentally governed by the hydrodynamic phenomenon known as the 'fluid-added mass' or 'virtual mass' effect. In the submerged state, as Inconel 690 tube oscillates, it must physically displace and accelerate the dense, incompressible volume of surrounding water. The inertia of this displaced fluid layer effectively acts as an additional kinetic mass physically appended to the structural mass of the oscillating tube.

Table 6. Max. recorded dynamic contact forces between Inconel 690 tube and smooth AVB under varying environmental conditions.

Excitation force [N]	40	50	60	70
Max. contact force air [N]	18.01	24.89	31.36	37.27
Max. contact force water [N]	21.39	28.93	36.31	46.48

According to fluid-elastic instability theory, this elevated virtual mass dramatically increases the total kinetic energy contained within the oscillating system, resulting in a more violent, higher-energy transfer during the millisecond collision event with the rigid AVB constraint.

Environmental influence on wear depth and micro-mechanical failure mechanisms

To comprehensively evaluate the impact of environmental medium on the degradation of Inconel 690 heat exchanger tubes, localised wear depths and micro-mechanical surface morphologies are systematically analysed and compared.

Profilometric extraction of wear depth curves along the axial centreline reveals a stark contrast between the two environments. As illustrated in the air environment wear profiles (Fig. 10), the maximal wear depth h_{max} escalates drastically and nonlinearly with the applied excitation load. At a baseline load of 40 N, the maximal depth is 12.75 μm. As the load increases to 50 N, 60 N, and 70 N, the wear depth surges to 17.84 μm, 23.93 μm, and a staggering 51.91 μm, in respect. This rapid deepening indicates severe stress concentration at contact boundaries under dry sliding conditions, leading to accelerated wall thinning.

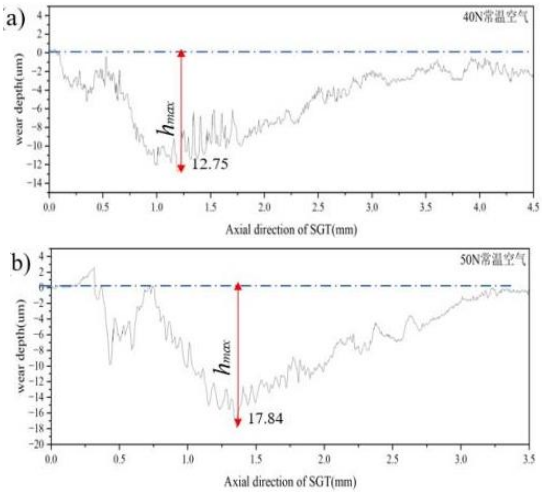

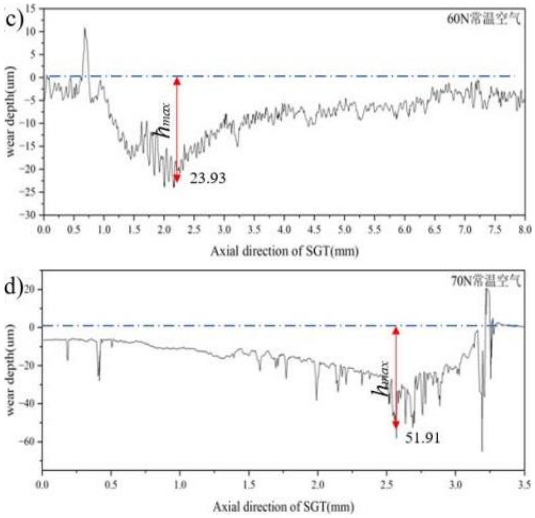

Figure 10. Quantitative analysis of thermal pipe wear under quasi-static vibration loads in ambient air: a)-d) 40-70 N.

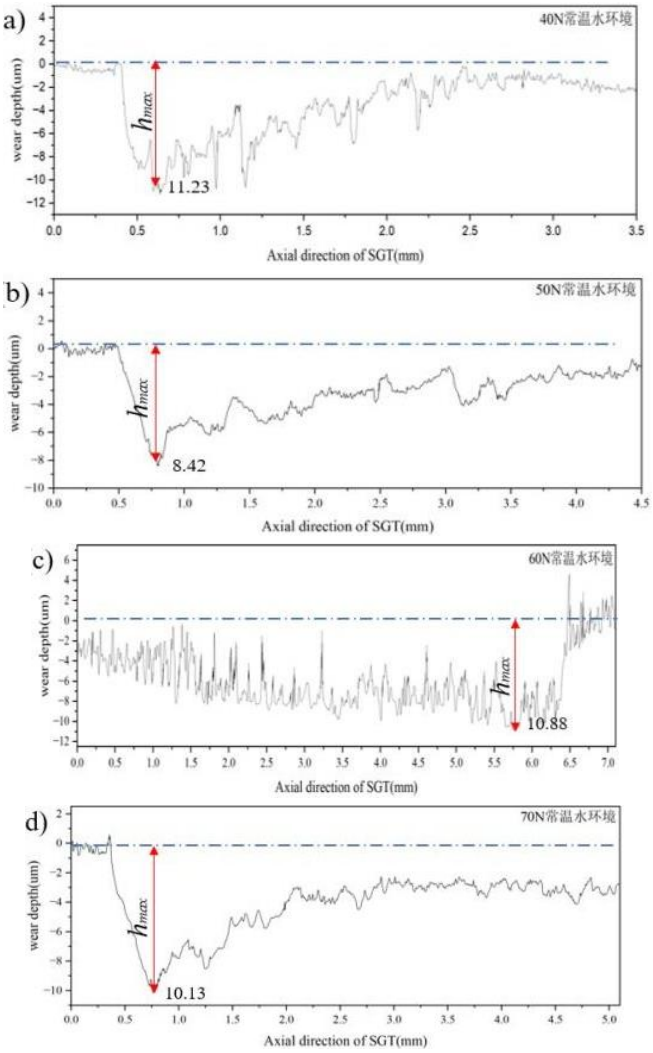

Figure 11. Quantitative analysis of heat exchanger tubing erosion under variable vibration loads in ambient water: a)-d) 40-70 N.

Conversely, the wear depth profiles obtained in the submerged water environment, Fig. 11, demonstrate a profound protective effect. Despite the increasing excitation loads from 40 to 70 N, the maximal wear depth remains remarkably

stable and shallow, recorded at 11.23 μm, 8.42 μm, 10.88 μm, and 10.13 μm, respectively.

To provide a more intuitive visualisation of this phenomenon, three-dimensional surface profilometry and two-dimensional optical micrographs are systematically compared across the 40 to 70 N load spectrum (as illustrated in Figs. 12-15). These topographies vividly capture the dimensional evolution of the wear scars. In the ambient air environment, the sliding distance (the width of the scar in the direction of tangential slip) expands significantly as the applied load increases, measuring 1.1 mm at 40 N, 1.3 mm at 50 N, and peaking at 1.7 mm for both 60 N and 70 N. Conversely, the fully submerged water environment effectively suppresses this lateral expansion. The sliding distances in water remain remarkably stable and constrained across the entire load spectrum, measuring only 0.9 mm, 1.0 mm, 0.9 mm, and 1.05 mm, respectively.

Interestingly, while the aqueous medium restricts radial wear depth and tangential slip distance, it promotes axial distribution of the wear area. Morphological analysis reveals that at higher loads (50, 60, and 70 N), the macroscopic lengths of wear scars in water (4.1, 5.4, and 4.6 mm, in respect) consistently exceed those generated in air (3.1, 4.6, and 3.1 mm, respectively). This morphological evidence confirms that the fluid medium provides critical hydrodynamic boundary lubrication. Instead of allowing the impact energy to gouge deeply into a concentrated local point, the lubrication relieves severe localised stress concentrations and redistributes the frictional energy longitudinally along the tube's axis, thereby preventing rapid, highly localised wall thinning.

Ultra-depth microscopic observations further elucidate the fundamental shift in tribological failure mechanisms. In the dry ambient air environment (Fig. 16), the worn surfaces exhibit severe degradation characterised by deep ploughing grooves laden with extruded metal remnants and massive spalling craters (delamination pits). These morphological features are indicative of intense two-body abrasive wear and high-cycle fatigue-induced delamination. The repeated dry impact-sliding induces severe plastic deformation and surface hardening, eventually causing the embrittled material to fracture and detach.

When the system is submerged in water (Fig. 17), the microscopic morphology changes dramatically. The massive spalling craters disappear, and the deep abrasive ploughing effect is visibly reduced, confirming that the aqueous lubrication effectively mitigates catastrophic fatigue delamination. However, the submerged wear scars are heavily blanketed by a compacted, irregular tribo-layer consisting of black and yellowish-brown oxidative debris.

This indicates that while the water environment reduces gross material removal, it traps the generated wear particulates within the contact patch. The continuous mechanical disruption by these trapped third-body particles, combined with the aqueous environment, facilitates a continuous cycle of mild abrasive ploughing and aggressive oxidative wear. Consequently, to further extend the structural lifespan of heat exchanger tubes and manage this trapped abrasive debris, the application of targeted micro-surface texturing on the anti-vibration bars is proposed as a necessary engineering intervention.

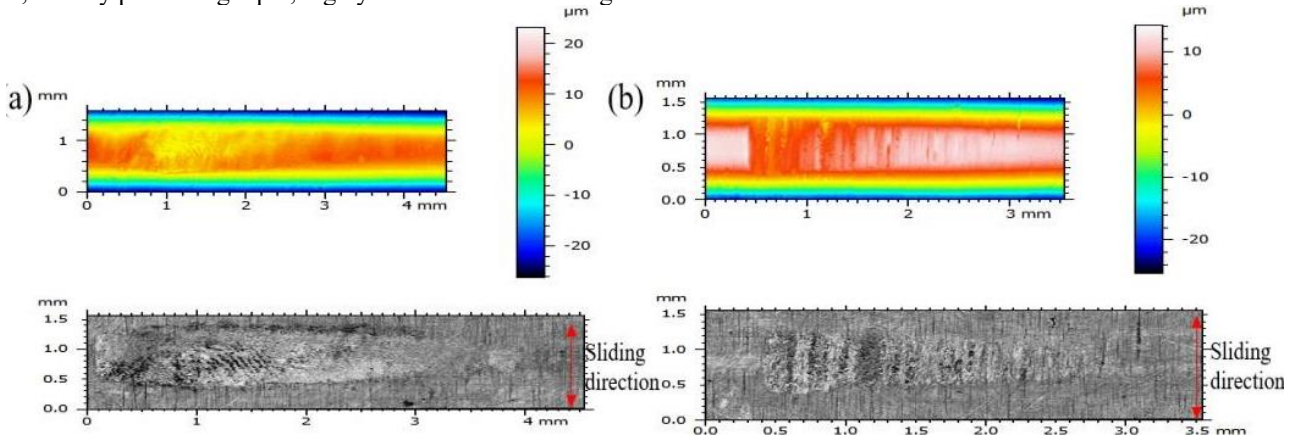

Figure 12. Impact wear morphology of 40 N: a) room-temperature air environment; b) room-temperature water environment.

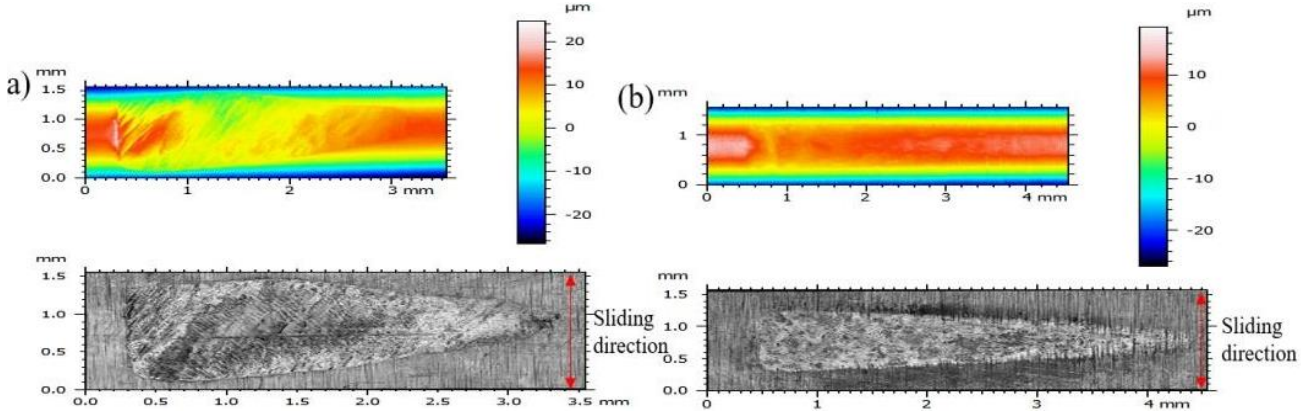

Figure 13. Impact wear morphology of 40 N: a) room-temperature air environment; b) room-temperature water environment.

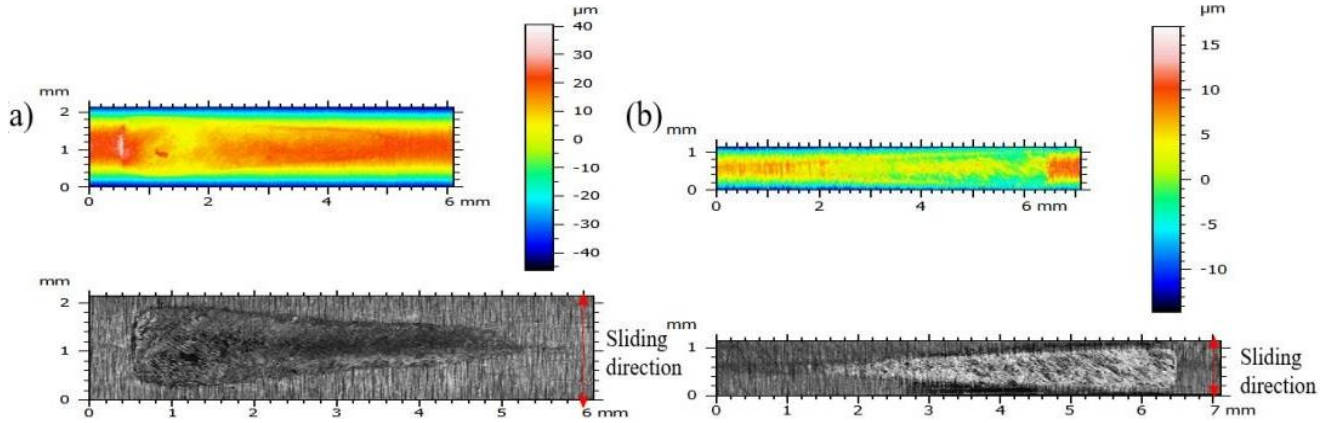

Figure 14. Impact wear morphology of 40 N: a) room-temperature air environment; b) room-temperature water environment.

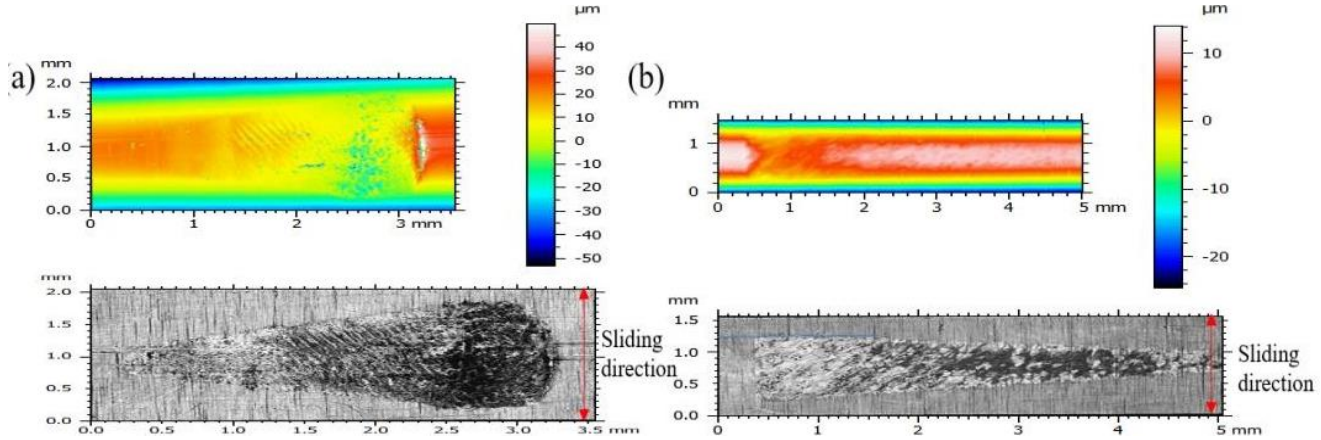

Figure 15. Impact wear morphology of 40 N: a) room-temperature air environment; b) room-temperature water environment.

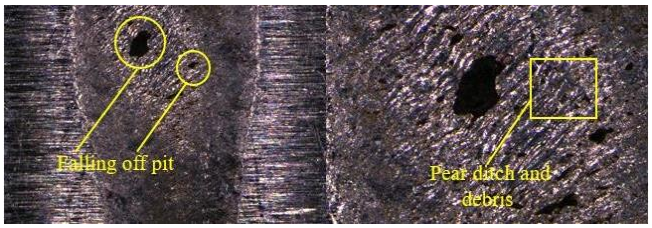

Figure 16. Abrasion marks morphology in a room-temperature air environment.

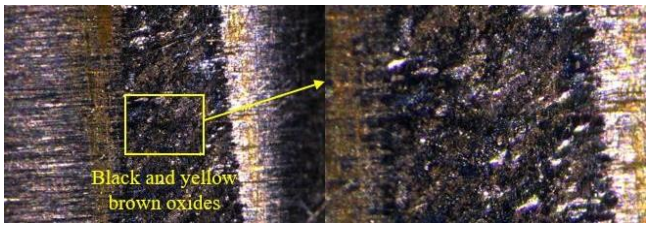

Figure 17. Abrasion marks morphology in a room-temperature water environment.

Micro-mechanical failure analysis via SEM and EDS

To further elucidate the wear mitigation mechanisms of micro-textured anti-vibration bars, a Phenom ProX Scanning Electron Microscope (SEM) equipped with Energy Dispersive X-ray Spectroscopy (EDS) is utilised to analyse the elemental distribution on the worn AVB surfaces.

As observed under the ambient air environment, Fig. 18, the worn surface of the smooth AVB exposes a massive amount of iron and exhibits numerous wear debris spalling craters. Crucially, these craters are highly enriched with oxygen, its content can reach 22.01 wt.%, indicating that the substrate experiences pronounced oxidative wear during the dry friction process.

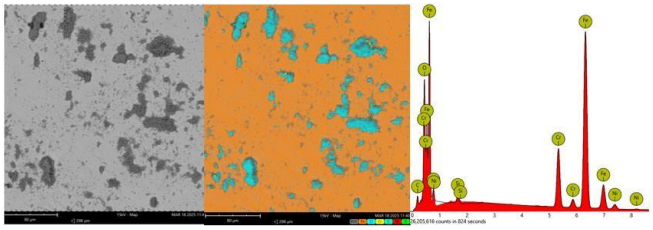

Figure 18. SEM analysis of worn anti-vibration bars-smooth anti-vibration bars in ambient air environment.

When submerged in room-temperature water (Fig. 19), the surface of the smooth AVB similarly develops extensive spalling craters. However, EDS analysis reveals that these pits contain a slight amount of oxygen alongside a significant accumulation of nickel. Given that the 405 stainless steel AVB substrate lacks intrinsic nickel, this confirms that material transfer occurs from the Inconel 690 heat exchanger tube to the support structure during the aqueous wear process. This transferred tube material transforms into wear debris and becomes compacted within the substrate's spalling craters, which are primarily generated by continuous fatigue wear. By comparing the oxygen mass fractions, the smooth AVB in air contains 8.01 % more oxygen than in water, demonstrating that oxidative wear is considerably more severe in the dry ambient environment.

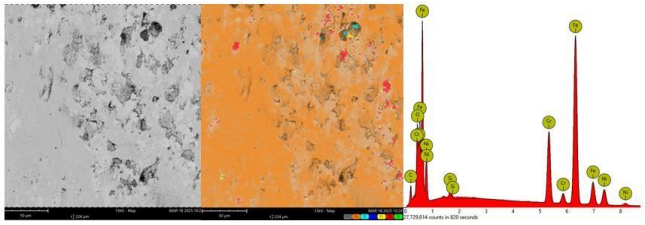

Figure 19. SEM analysis of worn anti-vibration bars-smooth anti-vibration bars in room-temperature water environment.

Conversely, on the micro-textured AVB operating in room-temperature water environment (Fig. 20), EDS mapping reveals a massive enrichment of oxygen heavily localised within the laser-ablated circular dimples. This concentrated oxidation may be attributed to the high energy density of the laser beam during fabrication, which rapidly elevates the metal surface temperature and accelerates localised oxidation reactions. Nevertheless, oxygen is also detected across the abraded plateau regions outside the dimples, confirming that oxidative wear continues to accompany the impact-sliding interaction in water. Despite this ongoing oxidative wear, the micro-dimples effectively capture and sequester the oxidised debris, thereby preventing severe abrasive degradation.

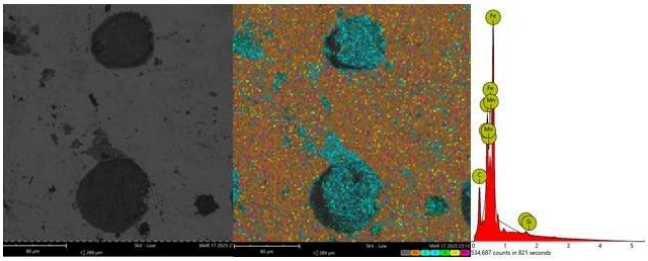

Figure 20. SEM analysis of worn anti-vibration bars-microtextured anti-vibration bars in room-temperature water environment.

CONCLUSIONS

Impact-sliding fretting wear experiments are conducted on Inconel 690 heat exchanger tubes against 405 stainless steel anti-vibration bars (AVBs) following femtosecond laser surface texturing. Tests are performed under varying excitation loads in both ambient air and fully submerged water environments to simulate authentic operational conditions and evaluate the efficacy of different micro-texture morphologies and densities. The following observations and conclusions are made.

The transition from ambient air to a fully submerged aqueous environment amplifies the maximal dynamic contact forces by up to 27.71 % due to fluid-added mass effects. However, the aqueous medium provides critical boundary lubrication that dictates the tribological behaviour. Consequently, the primary wear mechanisms fundamentally transition from severe high-cycle fatigue delamination and oxidative wear in air, to continuous mild abrasive and aqueous oxidative wear in water. Ultimately, this fluid-induced suppression of severe stress concentrations reduces overall volumetric material loss of the tubes by approximately 50 %.

Although femtosecond laser surface texturing enhances the localised microhardness of the 405 stainless steel AVBs by approximately 9.47 % due to rapid thermal quenching, its tribological efficacy is highly dependent on texture density. At a low surface area density of 10 %, the micro-textures fail to generate sufficient hydrodynamic fluid lift regardless of their geometric shape. Consequently, the sharp boundaries of the laser-ablated pits act as severe stress concentrators rather than protective reservoirs, paradoxically exacerbating the maximal localised wear depth on the opposing Inconel 690 tubes by up to 99.4 % compared to untextured smooth supports.

The implementation of circular micro-dimples at a high surface area density of 24.2 % yields the optimal tribological mitigation. This dense configuration effectively establishes high-capacity micro-reservoirs for debris sequestration and significantly enhances hydrodynamic lift. Together, these mechanisms reduce the total wear volume of Inconel 690 tubes by 87.9 % and decrease the maximal wall-thinning penetration by 72.8 %.

Ultimately, the substantial reduction in maximum wall-thinning (72.8 %) achieved through optimised micro-texturing directly addresses the critical vulnerability of steam generator tubes to FIV-induced perforation. This provides a highly effective, data-driven strategy to mitigate catastrophic leakage events - such as those observed in historical plant outages - thereby significantly enhancing the operational safety and long-term structural reliability of advanced nuclear power infrastructure.

REFERENCES

1. Abdellatif, H.H., Arcilesi D., Sabharwall, P., Bhowmik, P.K. (2024), *Accident event progression, gaps, and key performance indicators for steam generator tube rupture events in water-cooled SMRs: A review*, Prog. Nucl. Energy, 168: 105021. doi: 10.1016/j.pnucene.2023.105021
2. Benguigui, W., Benhamadouche, S., Beltran, F., Hassan, M. (2024), *Experimental and numerical contributions on flow-induced vibration in steam-generator-like tube bundles: A review*, Nucl. Eng. Des. 424: 113305. doi: 10.1016/j.nucengdes.2024.113305
3. Deng, H., Skaugen, G., Næss, E., et al. (2021), *A novel methodology for design optimization of heat recovery steam generators with flow-induced vibration analysis*, Energy, 226: 120325. doi: 10.1016/j.energy.2021.120325
4. Darwish, S., Mureithi, N., Hadji, A., Cho, M. (2024), *Wear work-rate measurement for different steam generator tube layouts in two-phase cross flow*, Nucl. Eng. Des. 424: 113226. doi: 10.1016/j.nucengdes.2024.113226
5. Guo, K., Tian, C., Wang, Y., et al. (2020), *An energy-based model for impact-sliding fretting wear between tubes and anti-vibration bars in steam generators*, Tribol. Int. 148: 106305. doi: 10.1016/j.triboint.2020.106305
6. Yin, M., Zhang, L., Huang, L., Long, J. (2024), *Investigation of the impact-sliding fretting behavior of 690 alloy tube using the finite element method*, ASME J Tribol. 146(11): 111502. doi: 10.1115/1.4065389
7. Gad-el-Hak, I., Mureithi, N., Karazis, K. (2024), *Vibrations of PWR fuel assembly under axial coolant flow and oblique impingement of jet cross-flow from LOCA holes*, Nucl. Eng. Des. 429: 113586. doi: 10.1016/j.nucengdes.2024.113586
8. Xin, L., Han, Y., Ling, L., et al. (2020), *The evolution of fretting wear behavior and damage mechanism in Alloy 690TT with cycle number*, Materials, 13(10): 2417. doi: 10.3390/ma13102417

9. Yin, M., Zhang, L., Huang, L. (2024), *Effects of salt spray duration on the fretting corrosion behavior of the inconel 690 alloy tubes*, Anti-Corr. Meth. Mater. 71(2): 191-203. doi: 10.1108/ACMM-11-2023-2919
10. Wang, G., Xiong, H., Zhou, S., Yin, M. (2025), *Impact-sliding fretting tribo-corrosion behaviors of Inconel 690 alloy pretreated with HTHP immersion for different durations*, Tribol. Int. 204: 110468. doi: 10.1016/j.triboint.2024.110468
11. Bian, W.W., Lu, Y.H., Kang, L.Z., et al. (2024), *The impact fretting corrosion behavior and damage mechanism of Inconel 690TT under different impact forces in high temperature pressurized water*, Corros. Sci. 240: 112507. doi.org/10.1016/j.corsci.2024.112507
12. Li, Y., Tan, W., Pei, W., Zhu, G. (2024), *The effect of NaCl concentration on impact-sliding fretting corrosion behavior of Inconel 690TT heat transfer tubes*, Anti-Corros. Meth. Mater. 71(5): 464-481. doi: 10.1108/ACMM-02-2024-2965
13. Xiong, H., Wang, G., Yin, M. (2025), *Damage response analysis combined with machine learning to investigate the effect of frequency on the impact-sliding fretting corrosion behavior of Inconel 690 alloy*, J Tribol. 147(4): 041701. doi.org/10.1115/1.4067662
14. Wang, H., Ma, Y., Bai, Z., et al. (2022), *Evaluation of tribological performance for laser textured surfaces with diverse wettabilities under water/oil lubrication environments*, Coll. Surf. A: Physicochem. Eng. Aspects, 645: 128949. doi: 10.1016/j.colsurfa.2022.128949
15. Yue, H., Schneider, J., Deng, J. (2024), *Laser surface texturing for ground surface: Frictional effect of plateau roughness and surface textures under oil lubrication*, Lubricants, 12(1): 22. doi: 10.3390/lubricants12010022
16. Rosenkranz, A., Grützmacher, P.G., Gachot, C., Costa, H.L. (2019), *Surface texturing in machine elements - a critical discussion for rolling and sliding contacts*, Adv. Eng. Mater. 21(8): 1900194.
17. Wang, H.-J., Huang, J.-D., Wang, B., et al. (2025), *Study on the tribological behavior of laser surface texturing on silicon nitride ceramic under water lubrication*, Lubricants, 13(1): 21. doi: 10.3390/lubricants13010021
18. Profito, F.J., Vlădescu, S.-C., Reddyhoff, T., Dini, D. (2017), *Transient experimental and modelling studies of laser-textured micro-grooved surfaces with a focus on piston-ring cylinder liner contacts*, Tribol. Int. 113: 125-136. doi: 10.1016/j.triboint.2016.12.003
19. Mao, B., Siddaiah, A., Liao, Y., Menezes, P.L. (2020), *Laser surface texturing and related techniques for enhancing tribological performance of engineering materials: A review*, J Manuf. Proc. 53: 153-173. doi: 10.1016/j.jmapro.2020.02.009
20. Lin, Z., Hong, M. (2021), *Femtosecond laser precision engineering: From micron, submicron, to nanoscale*, Ultrafast Sci. 2021: 9783514. doi: 10.34133/2021/9783514
21. Zschach, L.G., Soldera, F., Marzec, M., et al. (2025), *Laser texturing of AA2024 alloy: A simplified approach to improve corrosion resistance and achieve superhydrophobicity*, Surf. Coat. Technol. 513: 132487. doi: 10.1016/j.surfcoat.2025.132487
22. Piscitelli, F., De Palo, R., Volpe, A. (2023), *Enhancing coating adhesion on fibre-reinforced composite by femtosecond laser texturing*, Coatings, 13(5): 928. doi: 10.3390/coatings13050928
23. Vandoni, L., Demir, A.G., Previtali, B., et al. (2012), *Wear behavior of fiber laser textured TiN coatings in a heavy loaded sliding regime*, Materials, 5(11): 2360-2382. doi: 10.3390/ma5112360
24. Wang, Y., Liu, T., Luo, D., et al. (2025), *Study on the tribological and tribo-vibration characteristics of laser textured tapered roller bearings under full oil lubrication*, Industr. Lubr. Tribol. 77(2): 281-290. doi: 10.1108/ILT-09-2024-0357

© 2026 The Author. Structural Integrity and Life, Published by DIVK (The Society for Structural Integrity and Life 'Prof. Dr Stojan Sedmak') (http://divk.inovacionicentar.rs/ivk/home.html). This is an open access article distributed under the terms and conditions of the Creative Commons Attribution-NonCommercial-NoDerivatives 4.0 International License